

# Optical ghost modeling of the Maunakea Spectroscopic Explorer wide field corrector

Marc R. Baril<sup>\*a</sup>, Samuel C. Barden<sup>a</sup>, Damien J. Jones<sup>b</sup>, Will Saunders<sup>c</sup>, Jessica Zheng<sup>c</sup>

<sup>a</sup>Canada France Hawaii Telescope, 65-1238 Mamalahoa Highway, Kamuela, HI, 96743-8432 USA,

<sup>b</sup>Prime Optics, 17 Crescent Road, Eumundi, Queensland 4562, Australia,

<sup>c</sup>Australian Astronomical Optics, Macquarie University, 105 Delhi Road, North Ryde, New South Wales 2113, Australia

\*baril@cfht.hawaii.edu; phone 1 808 885-3139; cfht.hawaii.edu

## ABSTRACT

The Maunakea Spectroscopic Explorer (MSE) will target sources down to  $m_{AB} = 24$  with a signal to noise ratio  $> 1$  from the near UV to H-band. Among MSE's many science goals, this will allow the efficient spectroscopic follow-up of large imaging surveys anticipated from new facilities such as the Rubin Observatory. Given broadband AR coatings currently feasible for large optics, this poses a unique challenge in terms of controlling contamination from optical ghost reflections. We present exploratory work to identify telescope designs with optical ghost levels that satisfy the observational thresholds required for MSE. We also report on an initial estimate of scattering from the optics that indicates that it will have a minor impact on the accessible sky, does not drive the telescope design selection, but must be accounted for in science/sky fiber placement. The outcome of these studies is that a range of telescope configurations exist that allow MSE's target sensitivity to be reached without limitation from optical ghosts or scattering from the optics.

**Keywords:** Maunakea Spectroscopic Explorer, MSE, optical ghosts, wide-field corrector, scattering, ZOS-API

## 1. INTRODUCTION

The Maunakea Spectroscopic Explorer (MSE) will be a  $\geq 4000$  fiber dedicated spectroscopic facility aiming to complement the forthcoming generation of large-scale astronomical observatories<sup>1</sup>. Leveraging the Canada France Hawaii Telescope's excellent site on Maunakea, MSE sets a challenging requirement to robustly observe sources to  $m_{AB} 24$  in its lowest resolution mode ( $R \sim 3000$ ) with a signal to noise ratio (SNR) of 2 in one hour<sup>1</sup>. This places a tight constraint on contamination from optical ghosts and scattering originating from bright sources in the field. Specifically, to have minimal impact (10% of the continuum background), the combined ghost and scattering magnitude would have to be less than  $m_{AB} = 26.5$  for a zero-magnitude source.

This paper primarily addresses ghosting with scattering treated separately in Section 8. The main motivation for the design effort described here, was the finding that optical ghost levels in the MSE baseline design<sup>2</sup> would negatively impact survey efficiency. Specifically, complicated ghost prediction and avoidance algorithms would have to be applied, affecting hundreds of sources in denser star fields. In view of this, alternative telescope and wide-field-corrector (WFC) designs were studied to find solutions with better ghosting performance.

Optical ghosts can arise from any differing refractive index interface in the system, most problematically from air-glass interfaces. In rarer instances, reflections off lens surfaces can be reflected off mirrors, and be detectable at the focal plane. Restricting the discussion to the most common occurrence of reflections off multiple air-glass interfaces, the following factors impact the intensity of a ghost:

- The performance of the anti-reflection (AR) coatings
- The number of ghosting surfaces (typically, air-glass interfaces) in the design. For  $n$  air-glass surfaces there are  $\frac{1}{2}n(n-1)$  2<sup>nd</sup> order ghosts (ghosts involving two air-glass reflections). In certain cases, detectable ghosts may be generated off lens surfaces and reflected back to the focal plane by the telescope mirrors.

- The first order imaging properties of the surfaces generating the ghosts. This affects the size of the ghosts at the focal plane. The intensity of a ghost scales inversely with its size.

The spectral signature of a ghost is that of its source multiplied by the coating response for each reflection generating the ghost. Since the source is typically stellar continuum, and the coatings typically have one or more peaks, broad bands in the spectral bandpass are affected.

The relative surface brightness of a ghost in  $\text{mag}^{\prime\prime 2}$  relative to its source, here loosely its *delta magnitude*, can be estimated by dividing the source magnitude by the ghost area in  $\text{arc-sec}^2$  and multiplying by the reflectivity from each reflection. Such a first-order analysis for the prime-focus baseline MSE design<sup>2</sup> is shown in Figure 1, with either 2% (typical AR coating high) or 0.1% (typical AR minimum) reflectivity in the coatings, where each ghost reflection is assumed to involve the same reflectivity. The black vertical lines correspond to the main 2<sup>nd</sup> order ghosts present in the MSE baseline optical design. For a 2% reflectivity AR, all ghosts below  $\sim 0.5^\circ$  in size generate ghosts above the 26.5 mag threshold. At bandpasses where the coating performance is better (0.1% reflectivity), there are fewer problematic ghosts, however the one well-focused ghost remains above threshold (vertical line at  $\sim 1000 \text{ arc-sec}^2$ ).

Given this result, an investigation was launched to identify alternative MSE optical designs with better ghosting characteristics. Here we report on the three most successful designs: a prime-focus design using an M1 similar to the MSE baseline, a Cassegrain and a quad-mirror telescope.

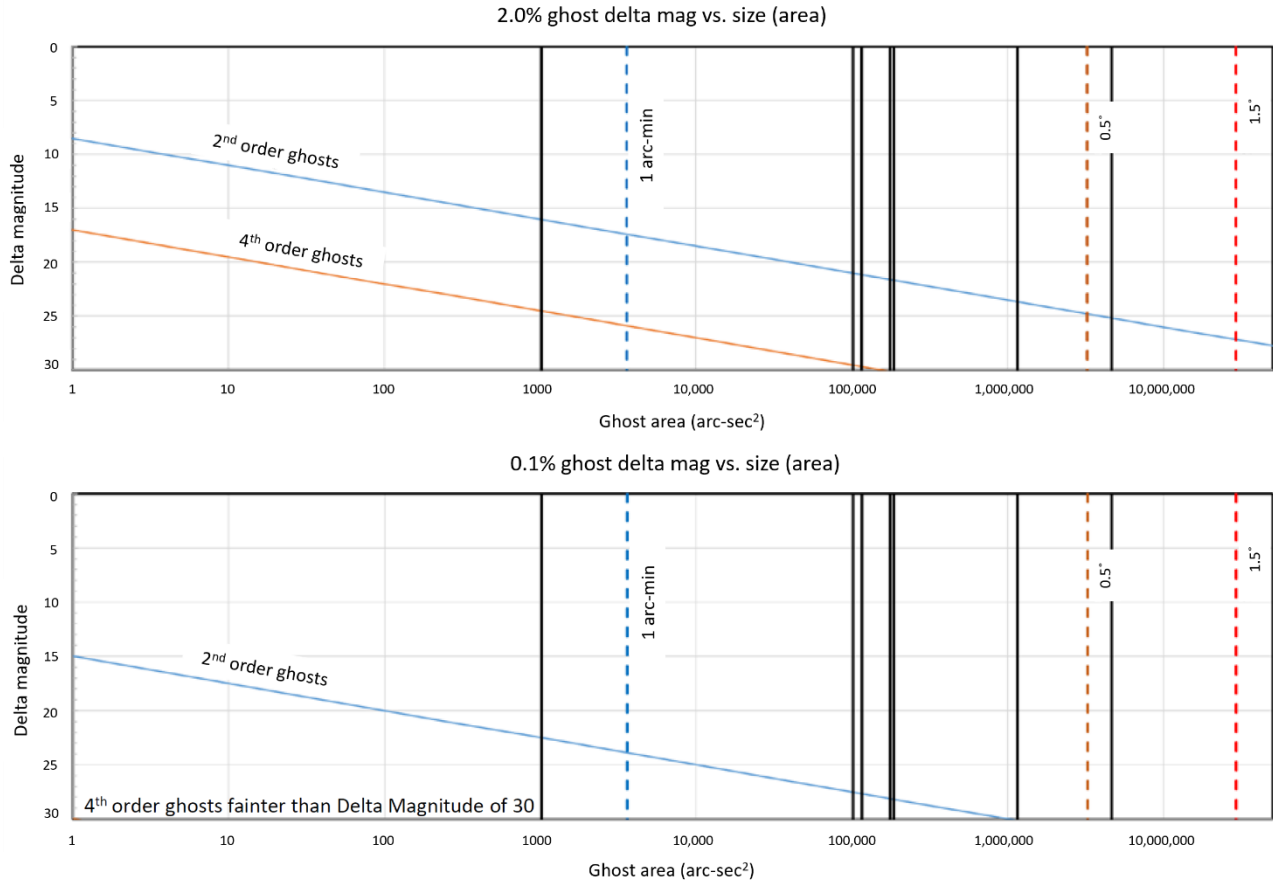


Figure 1: A first-order view of the ghost contributions in the MSE baseline prime-focus telescope design in terms of the ghost surface brightness ( $\text{mag}^{\prime\prime 2}$ ) relative to the source, or its “delta magnitude” versus the size of the ghost. Black vertical lines indicate the more prominent ghosts. The full MSE field is  $1.5^\circ$  in diameter.

## 2. THE TELESCOPE DESIGNS STUDIED

Briefly, the four telescope designs are described below, with simple ray diagrams shown in Figure 2. A closer view of the refractive components in each is shown in Figure 3.

**PF1:** The current baseline MSE prime-focus (PF) design, with a 5-lens corrector. This is a version of a design previously described by Saunders & Gillingham<sup>2</sup>, with improved performance at greater zenith distance (MSE’s internal “6w8” model). Atmospheric dispersion correction (ADC) is implemented by a shift and tilt of the entire WFC relative to a nearly stationary L2.

**PF2:** A 4-lens PF design, designated here as MSE-PF2, optimized specifically for optical ghost minimization, but from a facility support standpoint effectively identical to PF1.

**FC:** A 2-mirror “forward” Cassegrain design with the focal plane placed near the primary mirror (M1). This design is a modification of the Cassegrain design of Saunders & Gillingham<sup>2</sup> aimed at reducing the aspheric departure and curvature of the M1 to allow ELT style segments to be used, as in the PF designs. The FC can accommodate ~15700 tilting fiber spines<sup>3</sup> compared to the ~4300 of the PF designs and uses the same single lens tilt/displacement concept to implement the ADC as the PF designs.

**QM:** A quad-mirror modified Paul-Baker<sup>10</sup> design that supports up to 20,000 tilting fiber spines. The lenses serve almost entirely to implement the ADC functionality (classic counter-rotating elements). Like the FC, this design has been constrained to function with ELT segments. Also, this particular QM design minimizes the M2 and M3 size to allow these to fit through the existing CFHT mirror hatchway, which is necessary on a periodic basis for recoating the mirrors.

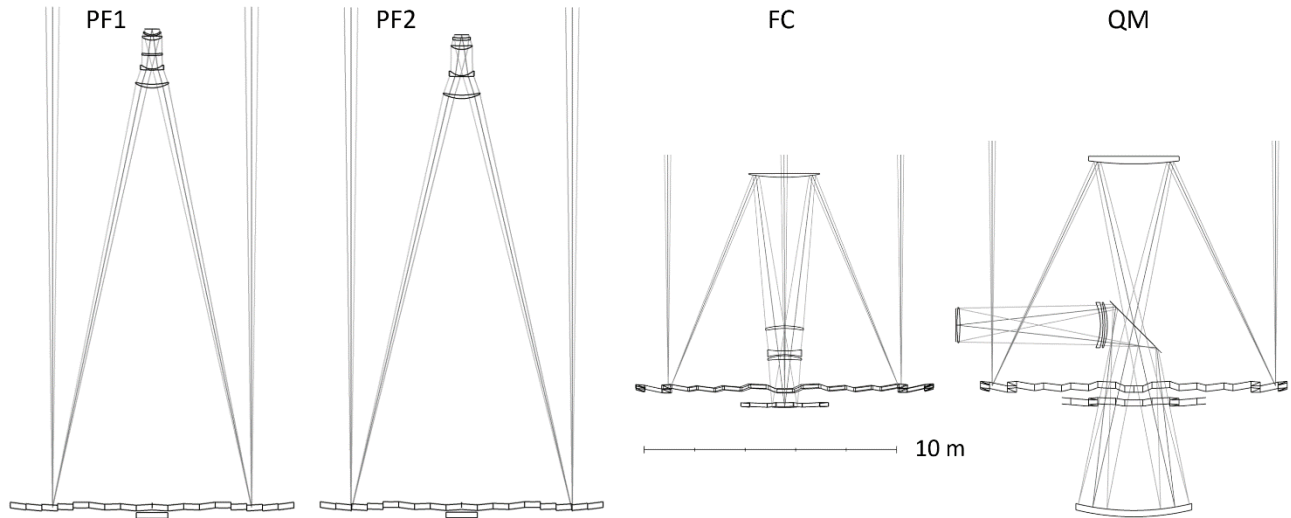


Figure 2: MSE telescope designs being compared for optical ghosting performance, drawn to the same scale. From left to right; PF1: MSE baseline prime-focus with 5-lens WFC, PF2: an alternative prime-focus with 4-lens WFC, FC: Cassegrain, and QM: quad-mirror. The v-3 design, which is more ghost-optimal is shown. The flat quaternary fold-mirror is perforated at the location of the intermediary focus.

While the PF2 design preserves the MSE prime-focus layout supporting ~4000 fibers, the FC and QM designs have longer focal lengths that allow for a four to five-fold increase in fiber count. The lower number of refractive surfaces near the focal plane for the FC and QM reduce overall ghosting levels. Also, in the case of the ADC design for the QM, there is significant room to adjust the surface curvatures of these low power lenses to control the focus of the ghosts at the FP. Note that no attempt was made to optimize these designs to minimize ghosts directly; instead, promising designs were independently verified for ghosts as they were proposed by the designers. It should be emphasized that although

the telescopes discussed here are near optimal in terms of the imaging requirements for MSE, they have not been subjected to extensive buildability studies, tolerancing, *etc.*

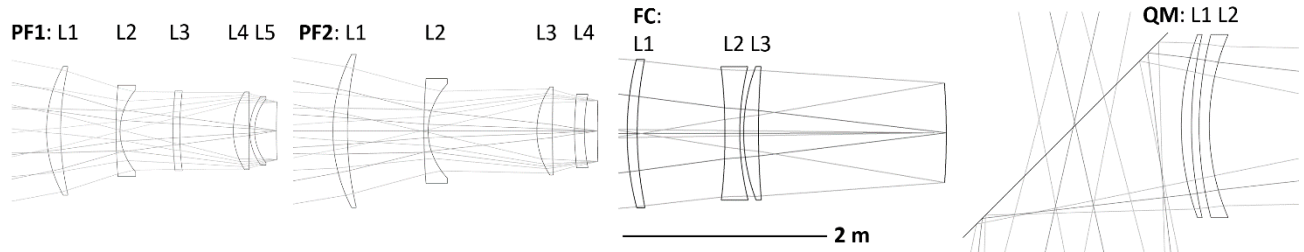


Figure 3: From left to right, a closer view of the lens elements of the, PF1, PF2, FC and QM (v-3) designs, all drawn to the same scale, with the focal plane on the right. Elements are all fused silica with the exception, in order of light travel; PF1: PBM2Y for lenses 3 and 5, PF2: FSL5Y for lens 3. The maximum lens diameters are PF1: 1.3 m, PF2: 1.46 m, FC: 1.4 m, QM: 1.8 m. The bi-convex L3 field lens of the QM design is not shown.

### 3. AR COATINGS

The choice of anti-reflection (AR) coatings in MSE is limited both by what can be applied to  $\sim 1$  m optics, and the wide  $3.6 - 1.8 \mu\text{m}$  bandwidth, with the best option currently being a single layer  $\text{MgF}_2$  with a solgel overcoat. Protected surfaces are assumed to be coated with  $\text{MgF}_2 + \text{solgel}$ , whereas exposed surfaces employ a single  $\text{MgF}_2$  layer. For ghost modeling, the same coating thicknesses were used in all the telescope designs, *regardless of glass type*, with the thicknesses roughly optimized for fused silica. These coatings are therefore neither completely optimized for glass type or manufacturability. The  $0^\circ$  incidence angle reflectivity of these coatings is shown in Figure 4. Ghost analysis was largely restricted to a wavelength of  $0.6 \mu\text{m}$ , which is the mid-band peak of reflectivity for both AR coatings. This level of accuracy is deemed sufficient for a comparative analysis between telescope designs.

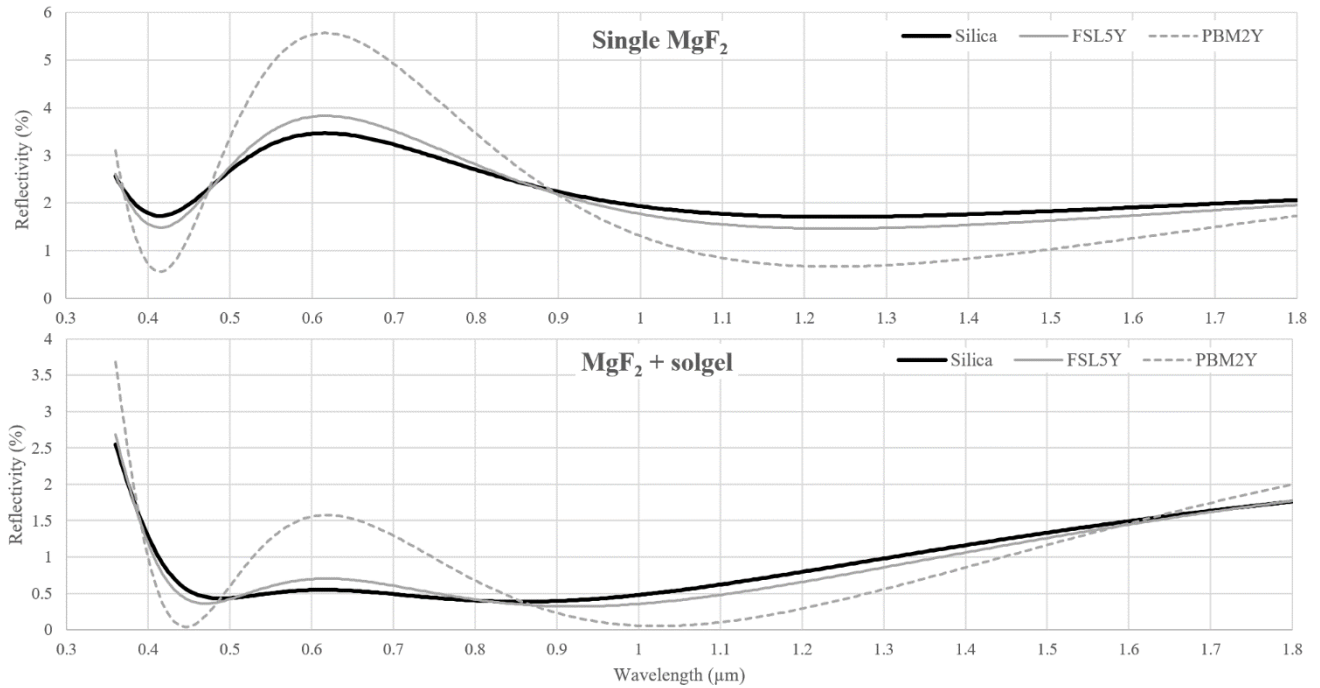


Figure 4: Model coatings used in the ghosting analysis.  $\text{MgF}_2 + \text{solgel} = 0.1275 \mu\text{m}$  solgel over  $0.1125 \mu\text{m}$   $\text{MgF}_2$ . Single  $\text{MgF}_2 = 0.225 \mu\text{m}$   $\text{MgF}_2$ . Coatings were roughly optimized for fused silica.

## 4. GHOST MODELING

Optical ghosts were modelled using Zemax OpticStudio™'s non-sequential module, with scattering disabled and with thresholds selected to detect the dimmest 2<sup>nd</sup> order ghosts (see further details in the appendix). Direct evaluation of the 4<sup>th</sup> order ghosts in the PF1 model indicated that even well-focused 4<sup>th</sup> order ghosts were negligible, as the estimate in Figure 1 would imply. An independent study of PF1's 2<sup>nd</sup> order ghosts using Photon Engineering's FRED™ package and the results agreed.

Over twenty models were investigated. For each, irradiance maps were produced for a minimum of 19 field angles of the source. Consequently, it became necessary to automate the data collection process. Python scripts were developed to control OpticStudio through Zemax's ZOS-API interface. This allowed hundreds of irradiance maps to be produced with very fine stepping of the source position, every 5" radially, or to scan over other parameters such as wavelength, with little intervention. Furthermore, ray-parameter filters could be automatically applied to the data during acquisition, and the output readily formatted as needed. The analysis suite developed allowed for consistency, and rapid turn-around in providing feedback on a proposed design.

Some additional details on the data collection:

- Delta-magnitude ghost irradiance maps were acquired at a 1"x1" spatial resolution, allowing direct conversion of detector plane pixel irradiance to surface brightness in mag/"<sup>2</sup>. This also avoids under-sampling the more focused ghosts which should be sampled at the spatial scale of the fiber input. Since the MSE fibers are nominally 1" in diameter, one should add 0.25 mag to the values read off the irradiance maps and plots.
- Rays with an angle of incidence at the focal plane exceeding 19° were rejected. This angle is the sum of the maximum ray angle for a fiber with nominal numerical aperture (NA) of 0.29, and the maximum fiber tilt (Echidna style fiber positioner) of 2.2°. Ghost rays steeper than this angle are rejected by the fiber.
- Since Zemax only defines a flat *detector object*, the detector viewer focus position was adjusted to account for field curvature, which has an impact on the intensity of the well-focused ghosts.
- The ghost irradiance measured within a pixel relative to the source power was computed from the irradiance sum in the pixel, divided by the sum of the irradiance over the detector. In all cases, the sum of the ghost power at the focal plane is negligible compared to the total incident power.
- Variations due to the ADC were neglected; in all cases the ADC was set to its zenith configuration.
- Scattering was ignored for the ghosting analysis.

The direct image of a point source at the focal plane (FP) is referred to in the following as the *source image*, or *SI*. Highly focused ghosts are referred to here as *image ghosts*. The term *following* or *opposed* ghosts refers to sign of angular magnification of the ghost relative to that of the SI. A following ghost has the same sign as the angular magnification of the SI, that is, it "follows" the SI on the FP as the field angle varies. The term *pupil-ghost* is used here loosely to refer to any ghost that is not an "image ghost".

## 5. GHOSTS IN THE MSE BASELINE DESIGN - PF1

Early analysis classified ghosts into three families broadly based on their origin. With five air-spaced lenses, 45 second-order ghosts are expected in PF1 (excluding ghosts involving the M1), the originating surfaces were only tracked for the brightest of these:

- Ghost 1 family: Four opposed ghosts, two of which are relatively well focused and have an angular magnification ~-10x that of the SI. They are not present beyond a source radial field angle of approximately 250". These ghosts originate from the combination of reflections involving both L1 and L5.
- Ghost 2 family: Consisting of the bulk of the pupil ghosts, originating from all the reflections not accounted for by families 1 and 3. Only eight of these ghosts are sufficiently small, 12' -16' in diameter, that they contribute significantly.
- Ghost 3 family: Two image ghosts that closely follow the SI. These originate from internal reflections in L3 and L5, individually.

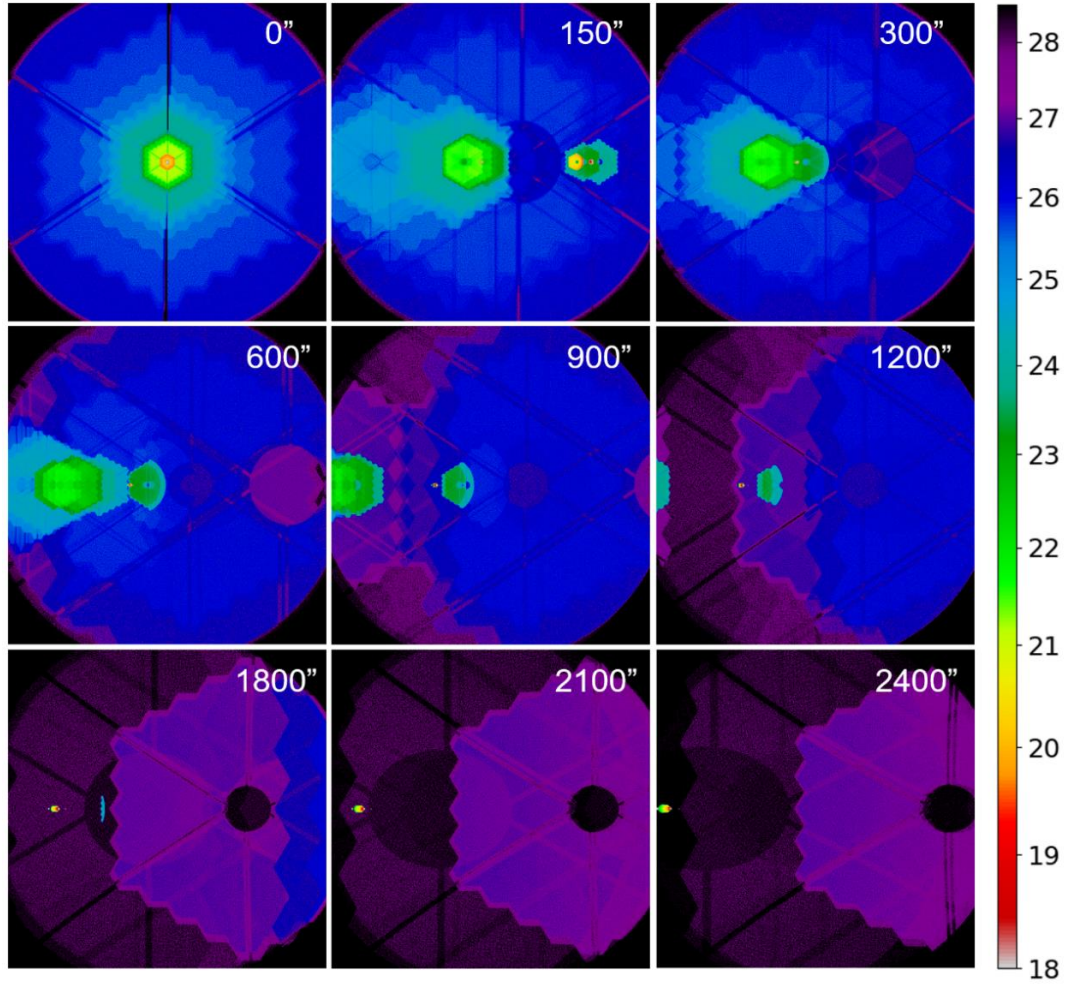


Figure 5: Irradiance maps for PF1 at different radial angles of the point source input. The SI is not visible at the scale of these maps which are 1.5° across. The color scale (right) is in relative to the source per square arc-second ( $\text{mag}/^{\circ 2}$ ). The ghost 1 family is visible only in the map for 150" field radius; beyond 250" this ghost moves off the field. Beyond the 1800" field radius, the two family 3 image ghosts dominate (small yellow and red feature moving to left with increasing field angle). Maps have been down sampled to 10"x10" pixel.

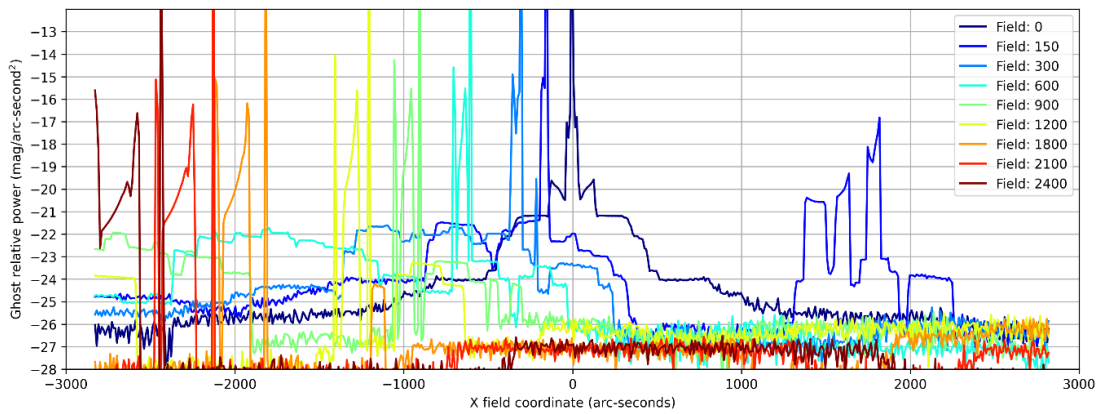


Figure 6: Horizontal cuts through the PF1 irradiance maps in Figure 5. The image ghost intensities are severely underestimated by the 10"x10" down-sampling, refer to Figure 7 and Figure 8 for a more accurate profile of the image ghosts.



The irradiance maps at the focal plane as a function of point source field position are shown in Figure 5. The family 1&2 ghosts individually affect a large FP area, but can be mitigated using relatively simple pointing restrictions, specifically:

- Avoid 5.5 magnitude or lower stars within a 100'' radius of the field center.
- Avoid 4.5 magnitude or lower stars within a 1000'' radius.
- Avoid 3.5 magnitude or lower stars within a 1200'' radius.
- Beyond the 1800'' radius, there are nominally no restrictions from the pupil ghosts.

Taken alone, these restrictions are expected to minimally impact survey efficiencies. However, the family 3 image ghosts, shown more closely in Figure 7, reach magnitudes up to 12.5 mag/''<sup>2</sup> (Figure 8). Although these ghosts individually affect a small area of the focal plane, many science target avoidance regions are needed because all stars brighter than magnitude 12.5 to 14 (source field angle dependent) produce objectionable ghosts. Near the galactic plane, the large number of target avoidance regions could significantly impact survey efficiency, limiting both useable field for both science and sky-background fibers. A direct demonstration of the impact of these ghosts on dense star fields is presented later.

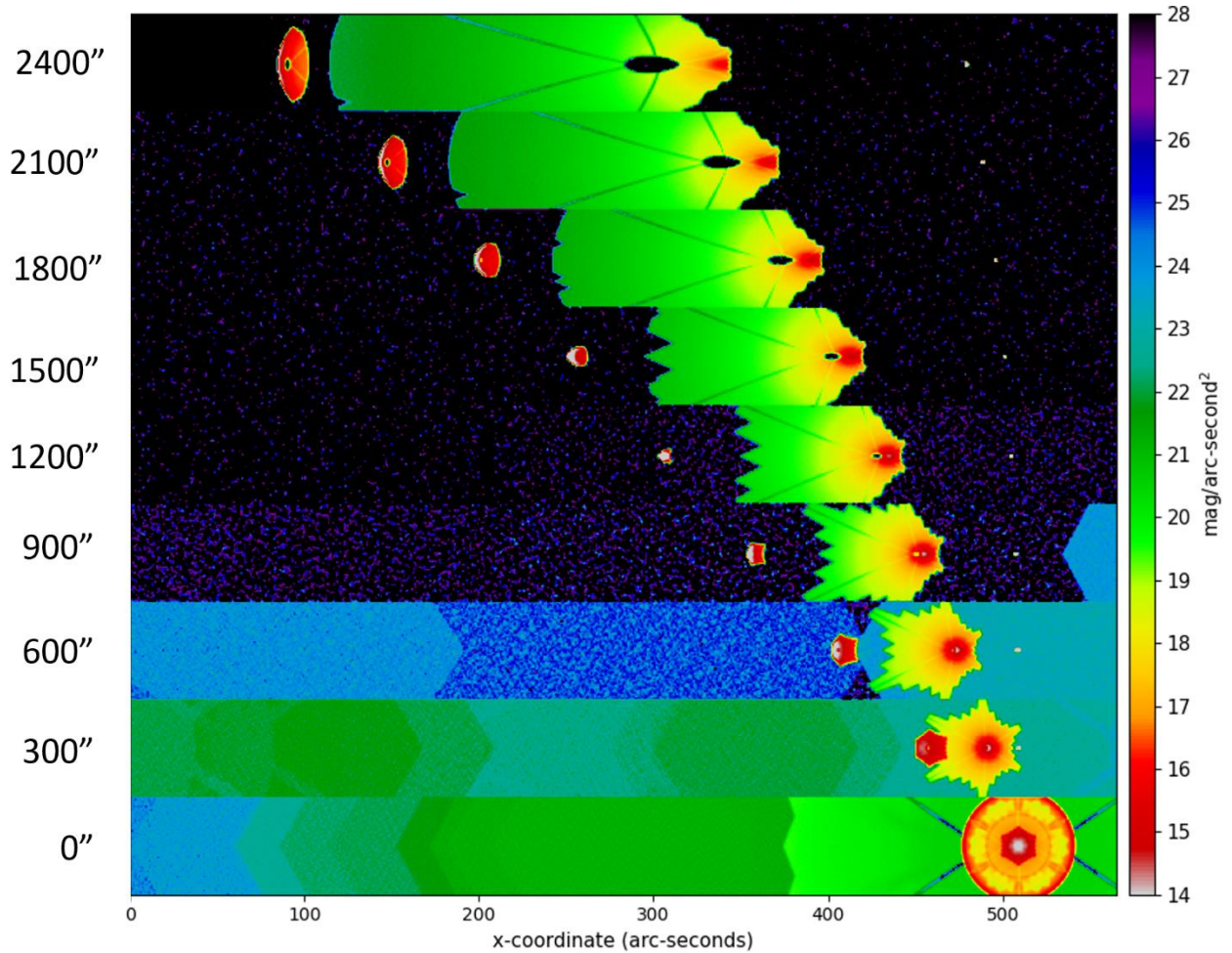


Figure 7: Region of interest in the PF1 irradiance map 550'' x 150'' in size, centered to the left of the source image (SI), and stacked vertically as a function of source field angle (noted on left). The SI can be seen ~50'' to the left of the right edge as a white dot, the bright features to the left of the SI are the family 3 image ghosts.

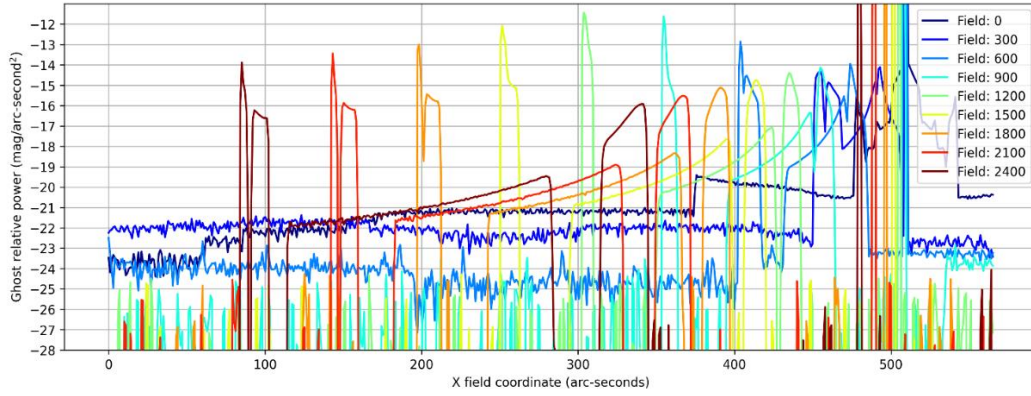


Figure 8: Horizontal cuts through the maps shown in Figure 7.

## 6. GHOSTS IN THE ALTERNATIVE DESIGNS

The image ghosts in PF1 are caused by reflections off the front and back surfaces of lenses that have near meniscus shapes, L3 and L5. The situation is aggravated if such a lens is located near the focal plane. For example, the image ghost from the meniscus L5 in PF1, is also the best focused. As a starting point, designs with near zero-power menisci close to the focal plane should be avoided, and the four-lens PF2 represents an improvement in this regard with respect to PF1. Figure 9 and Figure 10 show the significant improvement gained in the four lens PF2 WFC.

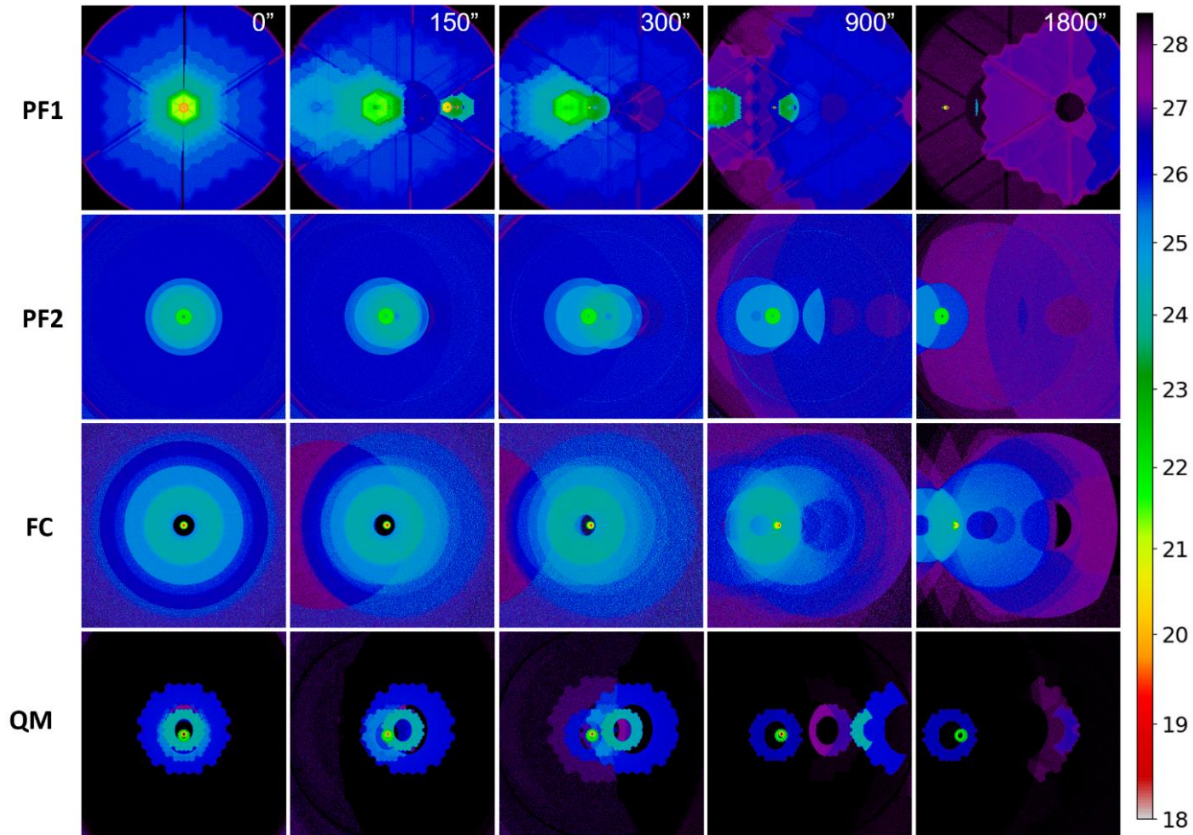


Figure 9: Full field ( $1.5^\circ \times 1.5^\circ$ ) irradiance maps as a function of source angular position (designated in top row) for the four designs; color scale is in  $\text{mag}/\text{arc}^2$ . A circular pupil has been used in the PF2 reduction although a segmented primary is expected.



In PF2 the brightest ghost arises from the near-meniscus shaped L4. This ghost has an intensity of  $22 \text{ mag/''}^2$ , relative to the source, 9.5 magnitudes dimmer than the brightest ghost in PF1. Consequently, ghost avoidance is expected to be considerably more tractable in the PF2 design versus the baseline PF1.

As for PF2, both the FC and QM show relatively minimal ghosting problems. Single following ghosts dominate, with  $22 \text{ mag/''}^2$  and  $20 \text{ mag/''}^2$  maximum delta-magnitudes respectively. At this ghosting level, other aspects of the optical design (focal plane size, image quality, lens element sizes, instrument placement, buildability...) are expected to drive the design selection. Although the PF2 design is nominally the “cleanest”, there is no practical significant difference between it and the FC and QM designs. The FC has the brightest ghost of the three designs – a following ghost with a delta mag peak near 18 (Figure 10). However, the peak of this ghost is  $\sim 18$  arc-sec from the SI. The light from the scattering halo due to dust contamination is expected to be comparable to this ghost at the same distance from the SI. In general, scattering levels the playing field between the PF2, FC and QM designs.

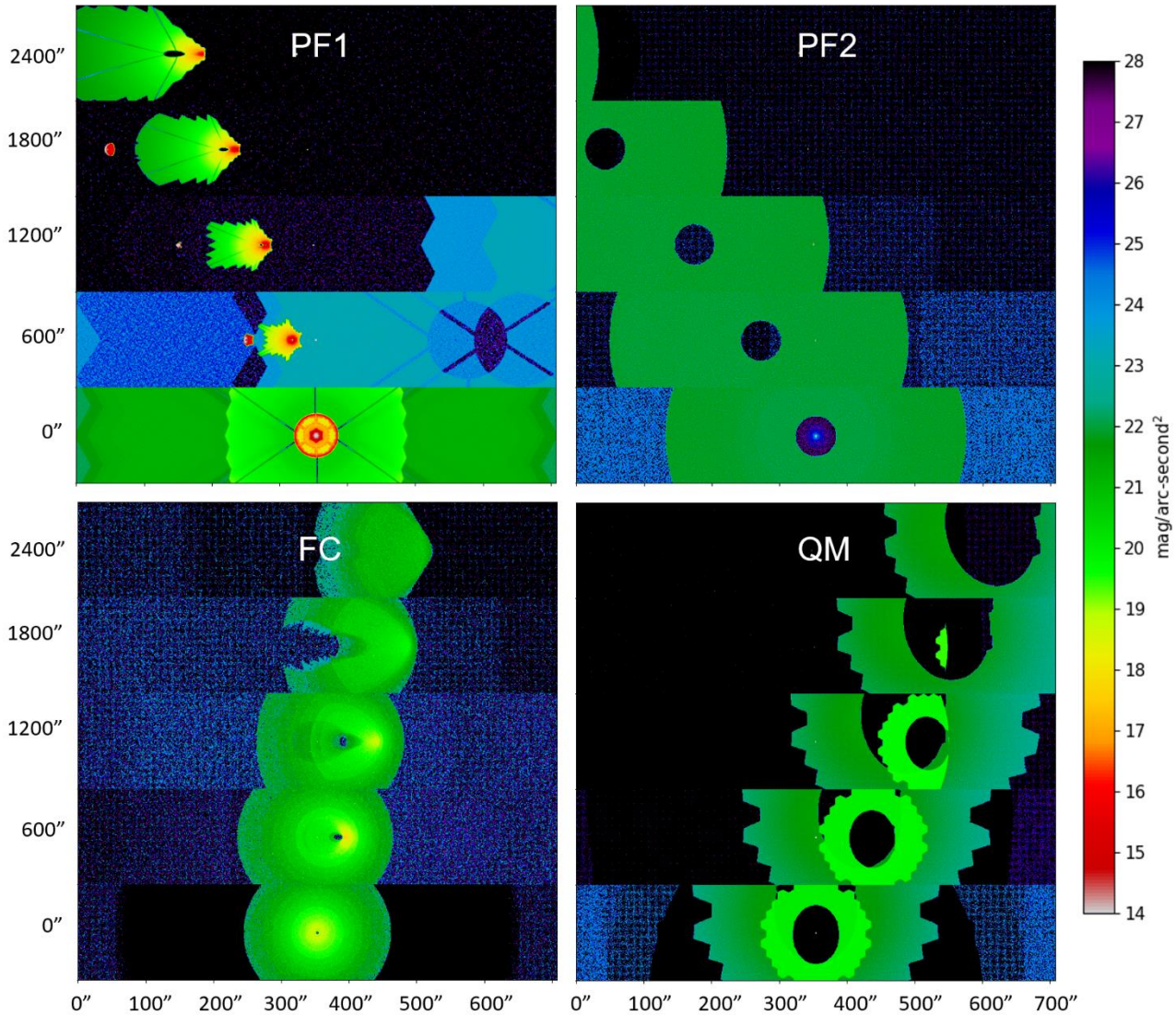


Figure 10: Irradiance maps in a  $700'' \times 140''$  ROI centered on the source image at five source field angles. The brightest ghosts in PF1 are below the intensity scale, at  $12.5 \text{ mag/''}^2$ , worst case.

## 7. GHOSTING IMPACT ON DENSE STAR FIELDS

Since many MSE science cases require observation of the galactic plane, one may ask whether the sum of the mid-sized (~100" to 500") ghosts sum up significantly in a dense star field? Although arguments based on star brightness distributions could be applied to broadly estimate the impact of ghosts on dense star fields, our analysis suite allowed for a direct computation of the effect. Ghost maps were generated at a fine spatial spacing of 5" along one radial direction of the field. These maps were then rotated and scaled according to the position and magnitude of stars in a star-field. The sum of these maps over the star-field gives the approximate integrated ghost contamination in the wavelength band selected for the stars. Minor inaccuracies occur from the limited spatial resolution (a 5" resolution for MSE requires the computation of 540 maps!) and the fact that the telescope designs are not axially symmetric (*i.e.* the near hexagonal pupil shouldn't rotate with the star position). However, this approach allows the ghosts from a field with thousands of stars to be simulated relatively quickly so that typical background levels can be estimated.

Star maps were generated from the ATLAS<sup>9</sup> catalog by selecting stars down to  $m_R = 18$ . An example of such a field is shown in Figure 11, it corresponds to a dense galactic field centered on the star HD187750 (summer north galactic plane), which is free of stars brighter than  $m_R=5.5$ . In this field, both the QM and PF2 are seen to be free of ghosts above the 26.5 delta-mag threshold. In the FC only the five brightest stars produce ghosts over threshold, and a limited area is affected.

In contrast, problematic ghosts abound in PF1; the total area affected remains small, indeed, few of the ghosts are spatially resolved in the rendering of Figure 11. However, assuming the dimmest level for PF1 brightest image ghost (delta mag 14), any star above  $m=12.5$  will produce a ghost above threshold. This star field contains 1790 stars brighter than  $m=12.5$  – a number of ghosts to track that is comparable to the number of fibers at the focal plane. Although it is conceivable to develop a sufficiently good optical model for the ghosts to accurately set target exclusion regions for these, it is by far preferable to design out the problem from the outset if such a complication can be avoided.

## 8. SCATTERING CONTRIBUTION

In addition to the application of target exclusion areas to avoid ghosting, it is expected that an exclusion radius will have to be applied near bright sources due to scattering from particulate contamination and surface micro-roughness in the telescope optics. To estimate the profile of the scattering halo from a point source, the following assumptions were made, largely following the reasoning applied in Hubbard's analysis for DKIST<sup>4</sup>:

- The scattering contribution from polishing micro-roughness was assumed to be the same for all optical elements. We note that the assumption of "print-through" of the surface figure to the coated surface is probably incorrect, and indeed, it has been noted that scattering off metallic coatings is highly dependent on the details of the coating process<sup>6</sup>. Nevertheless, we adopted this assumption as a starting point.
- As in Hubbard's analysis for DKIST<sup>4</sup>, a Harvey<sup>5</sup> model was used to model scattering due surface micro-roughness. Assuming a wavelength  $\lambda = 0.6 \mu\text{m}$ , a power-law exponent  $s = 1.5$ , and RMS surface roughness of  $\sigma = 20 \text{ \AA}$ , we use Hubbard's simplification that the scattering roll-off knee of the BSDF occurs at a very low angle (0.0001 rad is assumed), so that the Harvey  $b$  parameter is given by:

$$b \approx \frac{8\pi(s+2)}{100^s} \cdot \left(\frac{\sigma}{\lambda}\right)^2 = 9.8 \times 10^{-7}$$

The resulting Harvey model was converted to a near-equivalent ABg model for use in OpticStudio<sup>TM</sup>, with parameters:  $A=1.4 \times 10^{-4}$ ,  $B=10^{-6}$ ,  $g=1.5$ . The resulting total integrated scatter (TIS) for this BSDF is 0.17%.

- Scattering on enclosed surfaces was assumed to be dominated by the simple ABg BSDF model described above.
- Scattering off down-facing or side-facing exposed surfaces was assumed to be described by a BSDF consisting of a sum of the micro-roughness ABg model, and a Mie scattering model for dust contamination based on a "cleanliness-level" (CL) of 240 applied to the IEST1246E standard.
- Scattering off up-facing exposed surfaces was treated similarly to down-facing surfaces, with a CL of 500 assumed.
- It was assumed that the scattering PSF does not change significantly with field position. In the results reported here, the source was placed on-axis. Early modeling validated the adoption of this simplification.

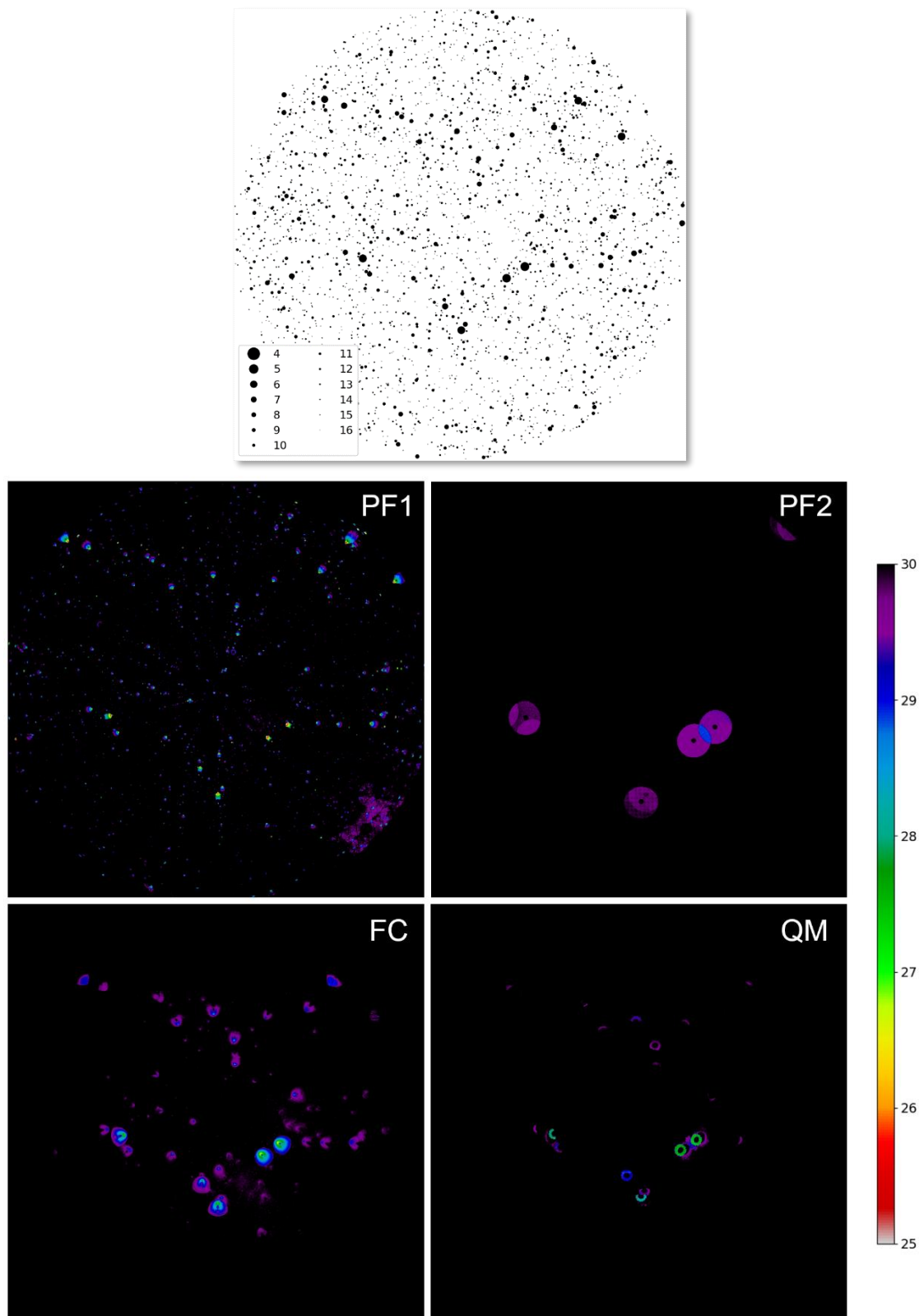


Figure 11: Ghosting map in  $\text{mag}/\text{arcmin}^2$  for a star field map centered on HD187750 (top), based on ATLAS R-band star magnitudes. The square field is  $1.5^\circ$  across. The five brightest stars are mag 5.5 to 6.8.

The Mie scattering model BSDFs were obtained using NIST’s “Modeled integrated scatter tool” (MIST) using the poly-disperse sphere “BRDF” (more accurately, BSDF) model<sup>7</sup>, applied in either transmission entering or exiting the transmissive medium, or in reflection, as appropriate. Specifically, the following four BSDFs described the entire system:

- A BRDF with CL=500 for upward facing mirrors. Total integrated scatter (TIS) at 0° incidence = 1.4%
- A BRDF with CL=240 for downward or side facing mirrors. TIS (as above) = 0.045%
- A BTDF with CL=240 for the case of light entering exposed lens surfaces. TIS = 0.017%
- A BTDF with CL=240 for the case of light exiting exposed lens surfaces. TIS = 0.015%

The maximum particle size used in generating the model in microns was set to the cleanliness level, as per IEST1246’s definition of the CL. The BSDFs generated using MIST were then fit to a sum of three ABg models to allow direct specification of the model in Zemax OpticStudio. To this sum of ABg’s, the microroughness ABg model was also added. Analysis was restricted to a 0.6  $\mu\text{m}$  wavelength. Note that the total integrated scatter (TIS) increases rapidly with the CL, so that upwards facing exposed surfaces strongly dominate the scatter.

The choice of CL is justified as follows. The particulate count in the CFHT dome is regularly monitored. Figure 12 shows the size distribution averaged over six particulate sensors mounted in the CFHT dome, over a 3-month period in 2021. The CFHT dome particulate counts vs. particle size are found to exhibit a higher power law exponent, 2.8, compared to the ISO 14633-1 cleanroom standard of 2.08. Nevertheless, it can be conservatively stated that the dome can be characterized as an ISO class 6 environment for the smaller particulate sizes. Applying this ISO class number to Fest’s<sup>5</sup> equation 5.11, using a fallout period of 360 hours (2 weeks), a  $\rho$  parameter of 80 (no air changes), an  $F_{\text{orient}}$  parameter of 1 (upward facing surface) and the standard particulate size slope of  $S=-0.383$ , a CL of  $\approx 500$  is obtained. The fallout period was set to two weeks because CO<sub>2</sub> sweeping of the exposed surfaces can reasonably be expected to be performed at a *maximum* of this period (this is the current typical cleaning period at the CFHT).

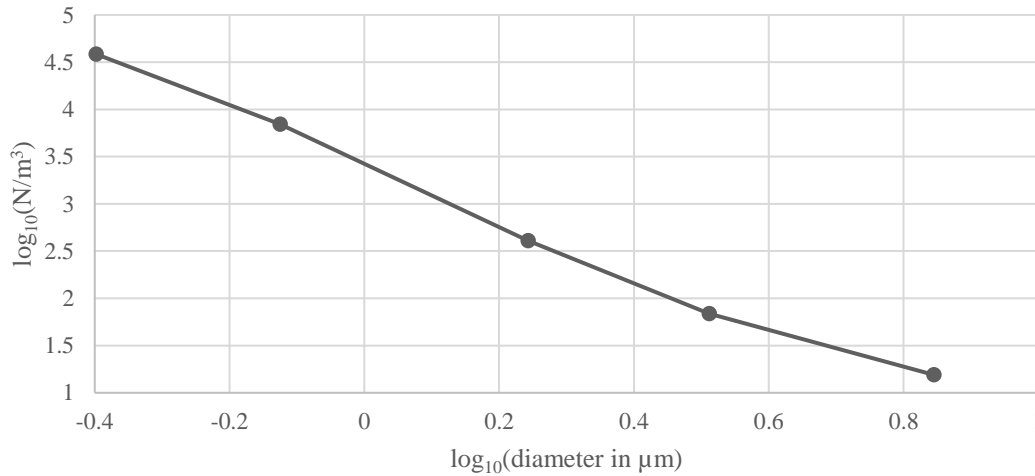


Figure 12: Particle size distribution from dust sensors located throughout the CFHT dome, with half the sensors located near the M1. Averaged over all sensors in the dome and over a 3-month time span. The slope of the power law is -2.8.

Calculating the CL with an  $F_{\text{orient}}$  parameter of 0.1 and 0.01, which corresponds to side-facing and downward-facing surfaces respectively, leads to an average CL of  $\approx 250$ . In fact, a CL of 240 was used for these surfaces since BSDF data had already been compiled for this value to allow comparison with Hubbard’s DKIST M1 analysis at  $\lambda=1 \mu\text{m}$ .

The scattering estimate obtained using the ABg sum models is shown for the four telescope designs in Figure 13. The FC design has a 1 magnitude edge over the other designs in terms of light scattered near the source image. The reason for this is the larger plate scale of the FC design compared to the PF designs combined with it having only one up-facing exposed surface. The two upward facing surfaces of the QM design negate the gains obtained from its large plate scale, however its performance remains competitive with the PF designs if the modest level of cleanliness assumed here can be maintained.



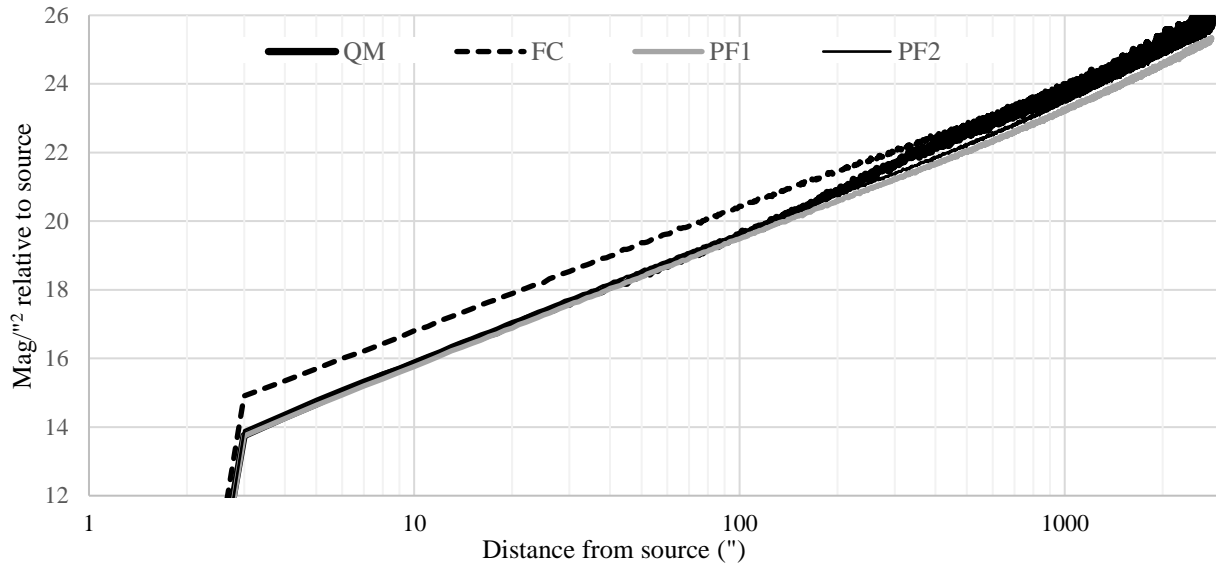


Figure 13: Estimated focal plane intensity of scattered light relative to the integrated intensity on the focal plane in  $\text{mag}''^2$  as a function of the radial distance from the source image center. Focal plane was spatially sampled at  $1'' \times 1''$  resolution.

Figure 14 shows the radial distance from the source image at which the scattering is below the  $26.5 \text{ mag}''^2$  threshold as a function of source magnitude, which directly provides the excluded patrol area of the fibers. The threshold radius closely follows a power law as a function of linear star intensity. The patrol radius is shown on the graph, serving as an indication of the source magnitude at which the fiber patrol area is significantly decreased by a nearby source. The PF designs are favored in this regard as the fiber density is considerably lower – an unavoidable tradeoff as the fiber density is increased. The difference in the patrol-radius/threshold-radius crossing magnitude {PF + FC} and QM designs is roughly an order of magnitude; at mag 7.1 and 8.3 respectively.

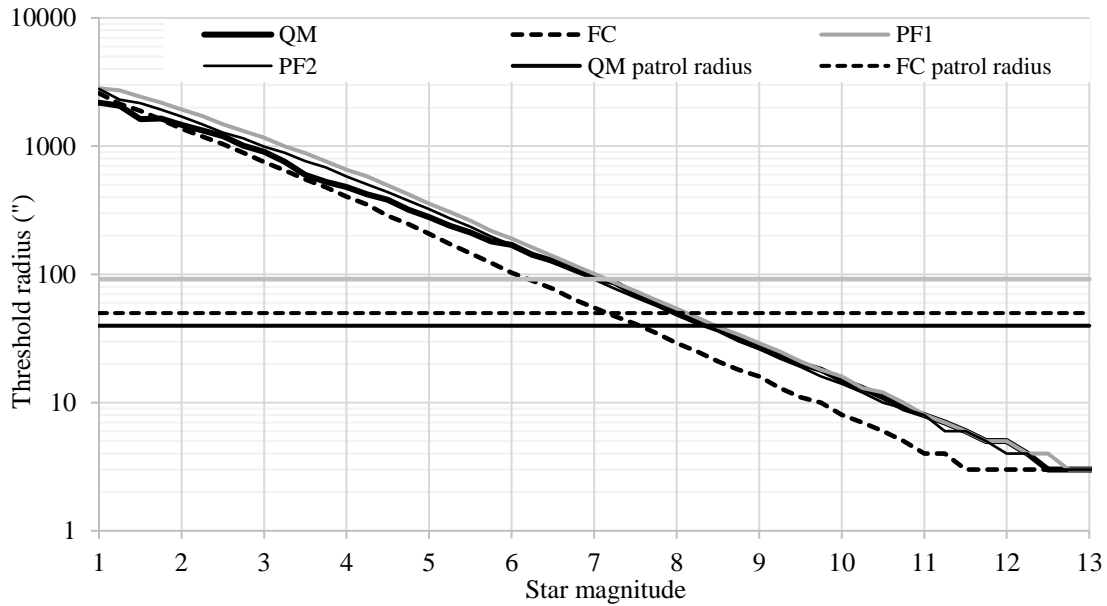


Figure 14: Threshold radius in arc-seconds above which the scattering halo is below the  $26.5 \text{ mag}''^2$  threshold as a function of star magnitude. The fiber patrol radius for each telescope design is shown using MSE's baseline Sphinx<sup>8</sup> fiber positioner.

Of more concern perhaps is the indication that stars below mag 3 will be difficult to accommodate in the MSE field directly (1000" avoidance radius vs. a 2700" radius field), with stars below mag 2 having to be kept out of the field entirely when survey requirements call for MSE's most stringent background thresholds. For stray light originating at the mirrors, the bulk of the stray light, it is not sufficient to place the bright source immediately off the focal plane as the scattering halo will still be detected. Detailed work is required to determine if the statistics associated with these limitations materially affect the science goals, especially on the galactic plane. Nevertheless, general conclusions can be made that suggest that most of these goals remain achievable:

- At the edge of the MSE field the scattering magnitude is near  $\sim 25 \text{ mag}''^2$  for all the designs, so 0<sup>th</sup> mag stars need be at most 1 field away (1.5°) to have no significant impact on the background. Only 12 stars with V-band magnitude  $\leq 1$  fall in this disturbance category.
- A simple solid-angle sum of the exclusion zones for stars to mag 10 in R-band indicates a fractional loss over the MSE accessible sky of; PF1: 0.45%, PF2: 0.35%, FC: 0.2%, QM: 0.3%. Of course, the fractional losses along the galactic plane and in bright galactic star clusters will be much larger than this, and a detailed study is warranted.
- The scattering irradiance vs. distance from the source follows a power law relationship. Further modeling can probably make use of this fact, for example to investigate effects due to the CL of the optics by simply scaling the scattering profile by the expected change in total integrated scatter.

It is also worth noting that the PF2, FC and QM designs have the advantage that the *optical ghosts generally follow the source, and thus the target exclusion zones for the ghosts generally overlap those due to scattering*. Not only does this reduce the total target exclusion zone area, but also it simplifies the avoidance algorithm. The FC, and especially the QM model have the distinct advantage of having dense sky coverage with fibers, which could in principle be used to more accurately estimate and correct background from scattered and ghost light on the science target.

At first glance, the avoidance algorithm for scattering may appear similar to what is needed to avoid the image ghosts in PF1. Practically, the situation is much simpler as, unlike the PF1 family 3 ghosts, scattering is always centered on the SI – one only needs to define a safe radius of exclusion centered on the scattering source, a function that varies weakly with field position.

In terms of scattered light, the FC presents a  $\sim 1$  mag advantage over the other designs due to its long effective focal length and minimal mirror count. Aside from this difference, this effect is seen to be generally “design agnostic” until the exposed optical surface count increases by a factor of two. For the more densely sampled field designs, the QM and FC, stray light from both ghosts and scattering is more difficult to avoid, however, the additional fibers allow the sky/nearby-source contamination to be better sampled, which is a distinct advantage of these designs.

To minimize scattering, the most important factor to control is the effective particulate area coverage (PAC), which should be kept below the  $\sim 1\%$  level implied in this analysis by the  $\sim 1.4\%$  worst case TIS adopted (*e.g.* Fest, ch. 5<sup>5</sup>). A moderately rigorous maintenance schedule will be required to maintain a TIS below this level. Enclosing the QM's M3 would be advantageous in maintaining cleanliness – in fact, the CL of 500 assumed here for the M3 is perhaps unlikely worst case that assumes that the M3 “sees” as much contamination as the M1. With the QM's M3 to M4 cavity enclosed, active ventilation would be necessary, however this would conveniently provide a means to control humidity in the volume defined by M3 and M4.

Since the overall loss of targetable sky due to scattering remains low at  $< 0.5\%$  of the entire MSE accessible sky in all designs, the main impact will be on science cases that target the galactic plane or bright open star clusters, and (probably minor) extra-galactic survey efficiency losses off the galactic plane. Future work will aim to define precisely how survey “tiling” of the actual MSE accessible sky is limited by the combined effects of ghosts and scattering.

## 9. CONCLUSION

Each of the designs considered represent a canonical telescope form: single mirror (prime focus), double mirror (Cassegrain) and triple mirror (3-mirror anastigmat). In each case an optical design was found with a workable ghosting performance for MSE. The leeway available in controlling the ghosts increases with mirror count, as the refractive element count decreases with the need to correct for fewer aberrations. The QM for example, can achieve the required imaging performance (neglecting atmospheric dispersion) with all but one lens, needed only in MSE's specific case to control pupil-centricity and field curvature to accommodate fibers. Consequently, considerable flexibility is available in designing an ADC for the QM that produces low ghost levels. At the other extreme, the PF2 design represents the best of at least three distinct WFC designs (with only the best two shown here), each with several sub-variants, where many of these had ghosts with the undesirable characteristics seen in PF1. The extensive design work to find a workable PF WFC, performed by two independently working optical designers, seems to indicate that an MSE PF design requires a minimum of 8 air-glass interfaces to achieve the required performance. In the absence of a simple, direct way to account for ghosts in the optimization merit function, successful low-ghost PF designs are by the far the hardest to "uncover". The best approach is to avoid known pathologies such as concentric surfaces near the focal plane, however, validation of each design with a full ghosting analysis remains inevitable.

It is important to emphasize that although the PF2 and QM represent the lowest-ghost solutions reported, we are confident that more optimal solutions for the FC exist which suppress its one modestly problematic image ghost. For example, a later version of the FC did not exhibit this ghost, but instead had a strong pupil ghost generated from a reflection in the corrector back to the M2 (excluding it as a contender in this review). Again, like the QM, the FC configuration affords much more flexibility to control ghosts than the PF.

Ultimately, the results indicate that the broad telescope design configuration are likely to be decided by factors other than optical ghosts. Similarly, scattering, which is largely independent of the design within a factor of  $\sim 2$ , will not be a discriminating factor between designs, although it must be controlled and accounted for when designing a science survey.

## APPENDIX: SETTINGS USED IN THE GHOSTING ANALYSIS

In nonsequential mode, Zemax OpticStudio™ defines a "minimum relative ray-intensity" (MRI) beyond which rays are ignored. Each parent ray splits into two child rays at every refractive interface, leading to a cascade of child rays tied to the original parent, with power tracked along each segment. If the MRI is not reached before either the maximum number of intersections (MSIR) or maximum number of segments per ray (MSPR) are reached, an error is thrown, and the entire ray cascade is discarded. If the errors are ignored, the result can be a severe underestimate of the ghost power, with entire ghost families disappearing as the minimum relative ray intensity parameter is reduced beyond what is appropriate for the MSIR and MSPR parameters. This led to some early unwanted "surprises" in our analysis.

For *second order ghosts, and the coatings used*,  $10^{-7}$  proved to be the optimum setting for the MRI parameter, maximizing computational efficiency while ensuring accuracy for the lowest ghost levels of interest. MSIR and MSPR were set to 1000 and 100,000. Comparison of Zemax calculations using a variant of the PF1 model described here against results obtained from FRED™ were found to be in agreement once the described settings were properly applied. We wish to thank Jessica Zhang for performing this independent analysis and lend confidence to our results.

## REFERENCES

- [1] McConnachie, A. W., Flagey, N., Murowinski, R., Szeto, K., Salmon D., Withington, K. and Mignot, S., "Science-based requirements and operations development for the Maunakea Spectroscopic Explorer", Proc. SPIE, 9906, 99063M (2016).
- [2] Saunders, W. and Gillingham, P., "Optical designs for the Maunakea Spectroscopic Explorer Telescope", Proc. SPIE, 9906, 990638 (2016).

- [3] Sheinis, A.I., et al.. “The Australian ESO positioner (AESOP) for 4MOST facility on the Vista Telescope”, Proc. SPIE, 9908, 9908306 (2016).
- [4] Hubbard, R., “M1 Microroughness and Dust Contamination”, ATST Project Documentation TN-0013, Rev. D.
- [5] Fest, Eric C., “Stray Light Analysis and Control”, SPIE Press, 2013.
- [6] Nelson, P. G., “An Analysis of Scattered Light in Reflecting and Refracting Primary Objectives for Coronagraphs”, Coronal Solar Magnetism Observatory Technical Note 4, Rev. 0.
- [7] Germer, T. A., Modeled Integrated Scatter Tool (MIST) [Computer Software]. National Institute of Standards and Technology. Retrieved from: <https://github.com/usnistgov/ScatterMIST/releases/tag/v4.21>.
- [8] Smedley, S., Baker, G., Brown, R., Gilbert, J., Gillingham, P., Saunders, W., Sheinis, A., Venkatesan, S., Waller, L., “Sphinx: a massively multiplexed fiber positioner for MSE”, Proc. SPIE, 10702, 107021M (2018).
- [9] Tonry, J. L., Denneau, L., Flewelling, H., Heinze, A. N., Onken, C. A., Smartt, S. J., Stalder, B., Weiland, H., J., Wolf, C., “The ATLAS All-Sky Stellar Reference Catalog”, The Astrophysical Journal, 867(2), 105 (2018).
- [10] Barden, S. C., Baril, M., Jones, D., “Exploration of a 14-meter, 1.5-degree field of view, quad-mirror anastigmatic telescope concept for wide-field spectroscopy and imaging”, Proc. SPIE, 12182-127 (2022).